Biophysical Journal Volume 107 September 2014 1236–1246

Article

Mechanical Aspects of Microtubule Bundling in Taxane-Treated Circulating Tumor Cells

MunJu Kim[1] and Katarzyna A. Rejniak[1,2,*]
[1]Integrated Mathematical Oncology Department, H. Lee Moffitt Cancer Center and Research Institute, Tampa, Florida; and [2]Department of Oncologic Sciences, College of Medicine, University of South Florida, Tampa, Florida

ABSTRACT Microtubules play an important role in many cellular processes, including mitotic spindle formation and cell division. Taxane-based anticancer treatments lead to the stabilization of microtubules, thus preventing the uncontrolled proliferation of tumor cells. One of the striking physical features of taxane-treated cells is the localization of their microtubules, which can be observed via fluorescent microscopy as an intense fluorescent band and are referred to as a microtubule bundle. With the recent advances in capturing and analyzing tumor cells circulating in a patient's blood system, there is increasing interest in using these cells to examine a patient's response to treatment. This includes taxanes that are used routinely in clinics to treat prostate, breast, lung, and other cancers. Here, we have used a computational model of microtubule mechanics to investigate self-arrangement patterns of stabilized microtubules, which allowed for the identification of specific combinations of three physical parameters: microtubule stiffness, intracellular viscosity, and cell shape, that can prevent the formation of microtubule bundles in cells with stabilized microtubules, such as taxane-treated cells. We also developed a method to quantify bundling in the whole microtubule aster structure and a way to compare the simulated results to fluorescent images from experimental data. Moreover, we investigated microtubule rearrangement in both suspended and attached cells and showed that the observed final microtubule patterns depend on the experimental protocol. The results from our computational studies can explain the heterogeneous bundling phenomena observed via fluorescent immunostaining from a mechanical point of view without relying on heterogeneous cellular responses to the microtubule-stabilizing drug.

INTRODUCTION

Microtubules (MTs), together with actins and intermediate filaments, constitute the main structural components of the cell cytoskeleton. MTs are important in a number of cellular processes: they help maintain cell shape and are involved in cell migration; they provide a platform for the intracellular transport of motor proteins; and they are essential in the formation of mitotic spindles that separate chromatids during cell division. Individual MTs are long, hollow cylinders composed of α- and β-tubulin dimers. The collective structure of MTs may, however, assume various configurations. The MT aster is a star-shaped structure in which the MTs radiate from a centrally located centrosome. The mitotic spindle that forms during cell division is composed of two asters located at opposite poles of the cell. The MTs emanate from these asters toward the spindle midzone and exert forces to separate chromosomes between two daughter cells. It is known that MTs in the neuronal cells form long longitudinal bundles stabilized by both microtubule-associated proteins and lateral cross links between microtubules formed via τ proteins (1,2). It has also been observed that in nonneuronal cells, some tubulin-stabilizing agents, such as taxane molecules, can cause MT bundling by themselves, without cross-linking from τ proteins (3–7).

The disruption of the MT structure and function that interrupts the process of cell division is an appealing potential mechanism of anticancer chemotherapeutic treatments (8–10). Taxanes, such as docetaxel, cabazitaxel, or paclitaxel, are a class of anticancer compounds that stabilize tubulins in the MTs, resulting in cell mitotic arrest and apoptotic death (11–13). It has been shown that in contrast to nontreated cells, in which MTs form uniform meshworks, the stabilized MTs in taxane-treated cells self-organize into bundles of long parallel structures detectable by immunofluorescence staining (14–16). Taxanes are widely used in clinics as chemotherapeutic agents to treat various tumors, including breast, head and neck, lung, ovarian, and prostate cancers (8,10,14).

With the recent advances in capturing and analyzing tumor cells circulating in a patient's blood system (16–22), there is increasing interest in using these approaches, called fluid-phase biopsies, to examine a patient's response to treatment. In particular, methods are being developed to test whether changes in intracellular composition of the circulating tumor cells (CTCs) correlate with the effects of taxane therapy (14,16,23). If successful, these procedures could be used to diagnose a patient's response to treatment and could be performed routinely in clinics.

Submitted April 16, 2014, and accepted for publication July 1, 2014.
*Correspondence: Kasia.Rejniak@moffitt.org
Editor: Leah Edelstein-Keshet.

0006-3495/14/09/1236/11 $2.00
http://dx.doi.org/10.1016/j.bpj.2014.07.009

In this article, we present the results of our computational investigation of intracellular biophysical conditions under which taxane-treated cells with stabilized MTs do not form bundles. The extensive simulation studies, with model parameters varied systematically over a broad range of physically relevant values, show that changes in MT stiffness, intracellular viscosity, and cell shape influence the final MT patterns. The resulting three-dimensional (3D) parameter space can be explored to determine which combinations of cell biophysical properties do not lead to bundle formation, shedding light on why not all taxane-treated cells show MT bundling. We also examined whether there is a difference in MT bundle formation between freely floating cells and substrate-attached cells, which may guide future refinement of experimental procedures and handling of CTCs so as not to bias the results of fluorescent imaging of cell MT patterns.

METHODS

Mathematical model

The mathematical model of MT bundle formation is based on the previously published model of the reorientation of the cytotoxic T-cell via the MT aster (24). We followed that work and modeled MTs as elastic rods with circular cross sections 25 nm in diameter clamped around the common centrosome (Fig. 1). MTs are capable of bending as a result of competition between elastic shape-restoring forces and viscous drag forces. There are, however, three main differences between the model presented here and the previously published model: 1), in this work, the cell shape is ellipsoidal (including the perfect sphere), to represent the deformability of CTCs floating in blood plasma, and the cells are unattached (but see MT bundles in suspended versus attached cells, where we investigate how cell attachment to the substrate influences bundle formation); 2), the number of MTs included in the model here is larger than in the previous model, and thus, the cell centrosome is defined differently (see The centrosome-organized MT aster); and 3), the MTs in our model are growing, and thus, special care is taken to ensure that the cell membrane is impenetrable (see MT growth); since we model the growth of MTs under the influence of stabilizing taxanes, the MT dynamic instability is neglected.

Cell structure

The cell boundary in our model is represented by an oblate spheroid and defined by the ellipsoid equation: $x^2/a^2 + y^2/b^2 + z^2/c^2 = 1$, with $a = b \geq c$. The lengths of the semiprincipal axes in the x and y directions are fixed at 5 μm ($a = b = 5$ μm), and c is varied from 2.5 μm to 5 μm to represent different cell shapes (Table 1; the cell-shape index is $S = a/c$). The ellipsoidal cell surface is assumed to be rigid and impenetrable. To elucidate the effect of taxane treatment on MTs, all other intracellular organelles, except the growing MT aster, are neglected (Fig. 1).

The centrosome-organized MT aster

We model the centrosome as a sphere 100 nm in diameter to which 92 uniformly spread MTs are clamped; the number of MTs is within the range used in other studies (25,26). The locations of the MTs were chosen based on the geodesic triangulation of the sphere. Starting with the icosahedron (20 triangles, 30 edges, and 12 vertices), each triangle was divided into nine identical smaller triangles, and MTs were attached to each of the final 92 vertices. Thus, the modeled MT aster contains 92 uniformly spread MTs, each clamped on the centrosome surface in the direction that connects the center of the centrosome and the vertex on its surface (Fig. 1). The rigidity of the MT, β, is one of the parameters varied in this study (Table 1).

MT growth

We assume that the cell is exposed to the taxanes that stabilize the MT structure. This leads to continuous MT growth at a speed of 5 μm/min, which is around the higher end of the reported values (27,28). Because of MT stabilization, the MT dynamic instability, which is the repeated growth and shrinkage of the MT free ends, is neglected. However, with increased length, the MTs need to bend to fit into a confined space restricted by the cell's impenetrable surface, and some MTs may not be able to elongate due to these spatial constraints. The bending process depends not only on MT stiffness, but also on the cell cytoplasmic viscosity, which is another parameter varied in our simulations (Table 1). The numerical procedure of MT bending is described below.

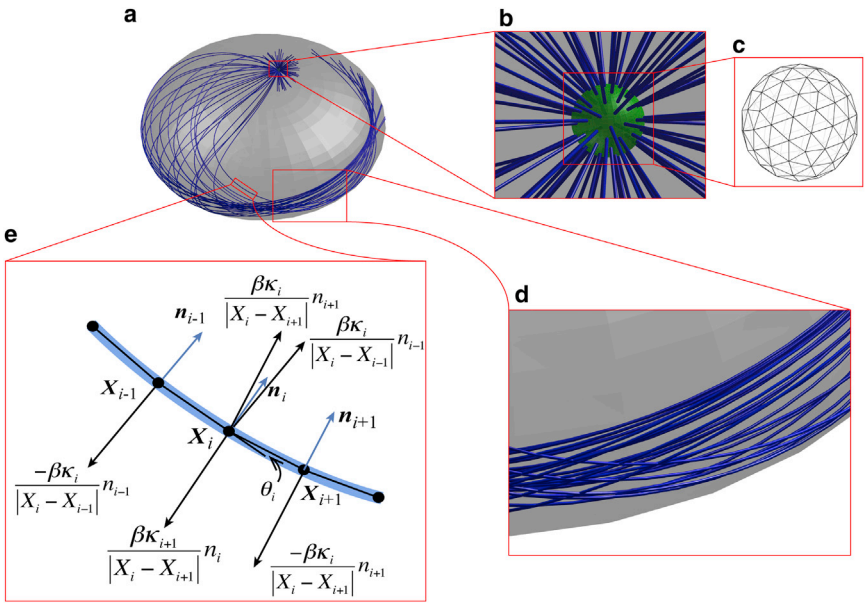

FIGURE 1 Schematics of a modeled cell. (*a*) A representative partial subset of MTs initiated from a centrosome inside a cell of ellipsoidal shape. (*b*) Magnification of a cell centrosome with a full set of MTs. (*c*) Geometrical representation of the centrosome with 92 vertices to which the MTs are clamped. (*d*) Magnification of an MT bundle consisting of long parallel MTs. (*e*) Schematic representation of balanced forces arising from MT bending rigidity. The thickness of all microtubules is exaggerated for visual purposes. To see this figure in color, go online.

TABLE 1 Model physical parameters

Symbol	Model parameter	Values used
S	Cell shape index (a/c)	1, 1.25, 1.42, 1.67, 2
β	Bending rigidity	5.2, 26, 52, 130, 260 pN·μm^2
η	Effective viscosity	8, 40, 80, 400, 800 pN·s/μm^2

Overall simulation procedures

In all simulations, the MTs were initiated at the surface of the centrosome (length zero) and were grown until the longest MT reached 18.8 μm (which we call the final MT length). This value was determined empirically to allow for the overlap of MTs growing from two opposite directions. This length was usually shared by 80% of MTs, and further growth of the MTs would not alter bundle formation. All cellular properties (cell shape, intracellular viscosity, and MT stiffness) were determined at the beginning of the simulation and were kept fixed thereafter. However, the MT shapes changed dynamically over time as a result of their physical interactions with the impenetrable cell surface, and these shapes were dependent on the bending rigidity and intracellular viscosity of the MTs (two complementary cases of MT growth and arrangement are shown in Fig. S1 and Movies S1 and S2 in the Supporting Material). The results were analyzed using the bundle index, a quantitative concept developed specially for this study (see Quantification of MT bundle formation: the MT bundle index) to measure whether the MTs self-arranged into a bundle.

Numerical implementation

Our numerical implementation closely followed that of the previously published work (24) in calculating the elastic deformation of MTs, including flexural rigidity (bending), axial rigidity (inextensibility or stretching), and clamping conditions. However, we developed additional algorithms for handling the increased MT length and for assuring cell-surface impenetrability.

The MTs are represented by the series of straight rod segments (cylinders 0.4 μm in length and 25 nm in diameter). Each rod is flexible along its axis and joined by torsional springs to model both the axial and flexural rigidities. The locations of the torsional joints, which are also the endpoints of rod segments (nodes), are denoted by $\boldsymbol{X}_i$ (Fig. 1). MT growth was implemented by adding one rod segment ($l = 0.4$ μm) every 4.8 s. As long as the newly added segment, $\boldsymbol{X}_k\boldsymbol{X}_{k+1}$, was contained within the cell surface, the direction of this segment was chosen to follow the direction of segment $\boldsymbol{X}_{k-1}\boldsymbol{X}_k$ to which the new segment was attached. However, if the distal end, $\boldsymbol{X}_{k+1}$, of the newly added segment fell outside the cell surface, we implemented the following algorithm to keep the whole MT inside the cell. We examined the penetration angle, that is, the angle between the outward normal vector to the ellipsoid surface at the penetration point and the direction of the added segment. If this angle was equal to 10° (π/18) or more, the new segment was rotated around the joint node $\boldsymbol{X}_k$ away from the normal vector within the plane that contained the outward normal vector, the $\boldsymbol{X}_{k-1}$ $\boldsymbol{X}_k$ vector, and $\boldsymbol{X}_k$ until node $\boldsymbol{X}_{k+1}$ came inside the cell surface and reached a distance of 12.5 nm (the radius of the MT cross section and the length at which the force creating impenetrability was activated) from the cell surface. If the angle was <10°, we did not allow the MT to grow, which reflected the difficulty of adding a new tubulin unit at the distal end of the MT in a confined space. In principle, it is possible to choose a threshold value of <10° for this angle. However, the resulting torque at the node just before the endpoint would be so large that a much smaller time step size would have to be used, thus significantly slowing the simulation process. This procedure is repeated for each MT.

Once the increment of all MT segments was determined, the shape and displacement of each MT (that is, the locations of all nodes $\boldsymbol{X}_i$) were dictated by three forces exerted on each node $\boldsymbol{X}_i$, that is, $\mathbf{F}^{bend}$, $\mathbf{F}^{stretch}$, and $\mathbf{F}^{impene}$. The first two arose from the elasticity of the MT, and the last was used to comply with the cell-boundary impenetrability condition. The locations of all nodes X_i were calculated by balancing the total force, $\mathbf{F}(\boldsymbol{X}_i) = \mathbf{F}^{bend}(\boldsymbol{X}_i) + \mathbf{F}^{stretch}(\boldsymbol{X}_i) + \mathbf{F}^{impene}(X_i)$, using the slender-body viscous drag force (24), that is,

$$\boldsymbol{X}_i(t+\Delta t) = \boldsymbol{X}_i(t) + \Delta t(\mathbf{F}^{p}(\boldsymbol{X}_i) + \mathbf{F}^{o}(\boldsymbol{X}_i)/2) \times \log(l/2r)/(2\pi\eta l), \quad (1)$$

where $\mathbf{F}^{p}$ and $\mathbf{F}^{o}$ are the parallel and orthogonal decomposition components, respectively, of $\mathbf{F}$. Here, l is the fixed length of the rod segment, r is its fixed cross-section radius, and η is its intracellular (effective) viscosity. The time-step size, Δt, was determined by bending rigidity to avoid numerical instability; thus, $\Delta t = 5 \times 10^{-5}$ s if $\beta = 26$ pN·μm^2, and Δt is inversely proportional to β. The forces that arose from elastic deformation were calculated as follows:

$$\mathbf{F}^{bend}(\boldsymbol{X}_i) = \beta\left(\frac{\kappa_i n_{i-1} - \kappa_{i-1} n_i}{|\boldsymbol{X}_{i-1} - \boldsymbol{X}_i|} + \frac{\kappa_i n_{i+1} - \kappa_{i+1} n_i}{|\boldsymbol{X}_{i+1} - \boldsymbol{X}_i|}\right), \quad (2)$$

$$\mathbf{F}^{stretch}(X_i) = k\left((|\boldsymbol{X}_{i-1} - \boldsymbol{X}_i| - l)\frac{\boldsymbol{X}_{i-1} - \boldsymbol{X}_i}{|\boldsymbol{X}_{i-1} - \boldsymbol{X}_i|} + (|\boldsymbol{X}_{i+1} - \boldsymbol{X}_i| - l)\frac{\boldsymbol{X}_{i+1} - \boldsymbol{X}_i}{|\boldsymbol{X}_{i+1} - \boldsymbol{X}_i|}\right). \quad (3)$$

Equation 2 constitutes a discrete implementation of the beam-bending equation at node $\boldsymbol{X}_i$; its schematic is shown in Fig. 1 *e* (the term related to $\kappa_{i-1}n_i$ overlaps with $\kappa_{i+1}n_i$). Here, κ_i is the MT curvature at $\boldsymbol{X}_i$, which is approximated by $2\theta_i/(|\boldsymbol{X}_{i+1} - \boldsymbol{X}_i| + |\boldsymbol{X}_{i-1} - \boldsymbol{X}_i|)$ (see Fig. 1 *e*), and n_i is the normal vector of the Frenet-Serret frame at $\boldsymbol{X}_i$ calculated based on $\boldsymbol{X}_{i-1}$, $\boldsymbol{X}_i$, and $\boldsymbol{X}_{i+1}$. Equation 3 is a discrete implementation of the linear spring equation at node $\boldsymbol{X}_i$. The axial rigidity constant, k, is 2000 pN/μm when β is 26 pN·μm^2, following Kim and Maly (24), and it is varied proportionally to β.

To enforce the impenetrability of the cell boundary by the MT nodes, we introduced the repulsive force $\mathbf{F}^{impene}(\boldsymbol{X}_i)$ if a node $\boldsymbol{X}_i$ approached the cell boundary within a distance of $\Gamma_0 = 12.5$ nm, similarly to the protocol followed by Kim and Maly (24). The force direction was inward normal to the cell boundary (ellipsoid) at the point from which the distance between the node and the ellipsoid was measured. The magnitude of the force was proportional to the violated length, with the proportionality constant $\eta/\Delta t$, which ensured that the cell-boundary impenetrability condition was strictly enforced regardless of the chosen time-step size (Δt). In a general form, this force is defined as

$$\mathbf{F}^{impene}(\boldsymbol{X}_i) = \frac{\eta}{\Delta t} H(\Gamma_0 - \Gamma(\boldsymbol{X}_i))(\Gamma_0 - \Gamma(\boldsymbol{X}_i))n_e, \quad (4)$$

where H is the Heaviside step function, $\Gamma(\boldsymbol{X}_i)$ is the distance between $\boldsymbol{X}_i$ and the cell boundary, and n_e is the inward vector normal to the cell boundary.

Note that we neglected any thermal fluctuations that may have potentially influenced MT shape and location. The theoretical estimation of MT persistence length was based on its Young's modulus, YI/k_BT, where Y is Young's modulus, I is the momentum of inertia, k_B is the Boltzmann constant, and T is the temperature (300 K)) is of the order of a few millimeters, much larger than the typical lengthscale used in this model.

Quantification of MT bundle formation: the MT bundle index

The MT bundle was identified as a collection of parallel MT filaments located close together over a significant portion of their length. Using this concept, we developed the following quantitative method to calculate

the MT bundle index and to assess whether the individual MTs had self-organized into the bundle structure.

At every MT node $\boldsymbol{X}_i$, except those located at the centrosome surface (the first node of each MT), we put a cylinder with the center at that node (Fig. 2 *a*, *large blue sphere*) and with the axis tangential to that MT (Fig. 2 *a*, *dashed line*). The height and diameter of the imposed cylinder were $2.5l$ and $1.5l$, respectively, where l was the length of the rod segment. Then we determined which rod segments from all other MTs are located inside the cylinder (Fig. 2 *a*, *thick red segments*). For each such rod, the angle θ between the segment and the cylinder axis and the distance d between the segment's center point and the cylinder axis were calculated and counted toward the value of the local weighted count (WC). The definition of the WC at X_i is given in Eq. 5, where the weight functions penalizing nonparallel and distant segments are depicted in Fig. 2 *b*.

The WC values is given by the equation

$$WC(\boldsymbol{X}_i) = \sum_{\substack{segments \\ in\ cylinder}} W_1(\theta)W_2(d) \qquad (5)$$

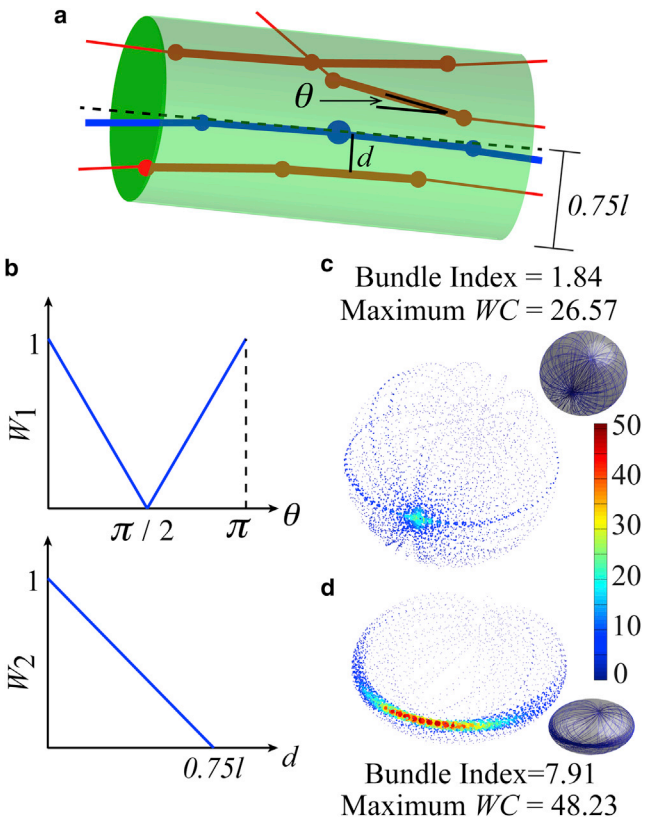

FIGURE 2 Schematics of the MT bundle index method. (*a*) Schematic diagram of components contributing to the WC value at a single node: For a given node (*large blue sphere*) joining two MT segments (*blue lines*), a cylinder with an axis tangential to that node (*dashed line*) is defined, and rod segments (*five thick red lines*) contained within the cylinder contribute positively to the WC. (*b*) Graphs of two weight functions, $W_1(\theta)$ and $W_2(d)$, where $0.75l$ is the cylinder radius and l is the rod length. (*c* and *d*) Examples of the WC and bundle index values for $S = 1$, $\beta = 26$ pN·μm^2, and $\eta = 8$ pN·s/μm^2 (*c*) and $S = 2$, $\beta = 26$ pN·μm^2, and $\eta = 8$ pN·s/μm^2 (*d*). Individual dots represent the WC at each node, with dot size proportional to the WC value; the WC color scale is identical in both cases. (*Insets*) Actual configurations of the MTs in each case. To see this figure in color, go online.

The MT bundle index for a given cell was then taken as the average of all the weighted counts at all nodes of all MTs and was defined as

$$\text{Bundle index} = \frac{\sum_{all\ nodes} WC(\boldsymbol{X}_i)}{\text{Total number of rod segments}} \qquad (6)$$

Two different MT arrangements are shown in Fig. 2, *c* and *d*, with their corresponding local WC values and bundle indices. Note that local accumulation of MT segments (Fig. 2 *c*) can result in a high WC value, but does not lead to a high bundle index, since high WC values are sporadic, whereas a high bundle index (Fig. 2 *d*) requires high WC values along individual MTs. Additional examples are discussed in section S1 of the Supporting Material and Fig. S1.

RESULTS

Analysis of the 3D parameter space of MT bundle formation

All simulations discussed in this section were performed under the assumption that cells were in suspension (like CTCs in blood) and were exposed to taxane-based drugs in concentrations that stabilized the tubulin, leading to persistent MT growth. Our main goal was to investigate how the internal physical properties of a cell—MT stiffness (β), intracellular viscosity (η), and cell-shape distortion (S)—influence the formation of MT bundles. Very diverse values of these intracellular properties were reported in the experimental literature (four orders of magnitude of difference in MT stiffness (29,30) and five orders in intracellular viscosity (31–33); see section S2 in the Supporting Material); however, there are no reports on both MT stiffness and intracellular viscosity measured in parallel in the same tumor cells or cell lines. Therefore, we analyzed a broad range of parameter combinations and considered five values of β (5.2–260 pN·μm^2) and five values of η (8–800 pN·s/μm^2), all within the ranges reported in the experimental literature. We also considered five different spherical shape deformations under flow, which was denoted by cell-shape index S, (where $S = 1$ represents the perfect sphere and $S = 2$ corresponds to a flattened spheroid). Finally, we ran all simulations starting with zero-length MTs, so as not to bias the final MT arrangement by a predefined initial configuration. However, we analyzed cases initiated with already formed MT asters and showed that MT bundle formation does not depend on initial MT length (sections S3 and S4 in the Supporting Material). Of 125 possible combinations of these parameters, we simulated 37 cases until a clear correlation between model parameters and MT bundle formation was observed. These results are summarized in Fig. 3.

The 37 simulated results are shown as a bar graph (Fig. 3 *a*), with the bars sorted by bundle index (Fig. 3 *a*, *bar height*) and the three color families indicating the values of the three associated parameters (*red shades*, cell shape index; *green shades*, intracellular viscosity; and *blue shades*, MT stiffness). The same results are placed in the 3D parameter space

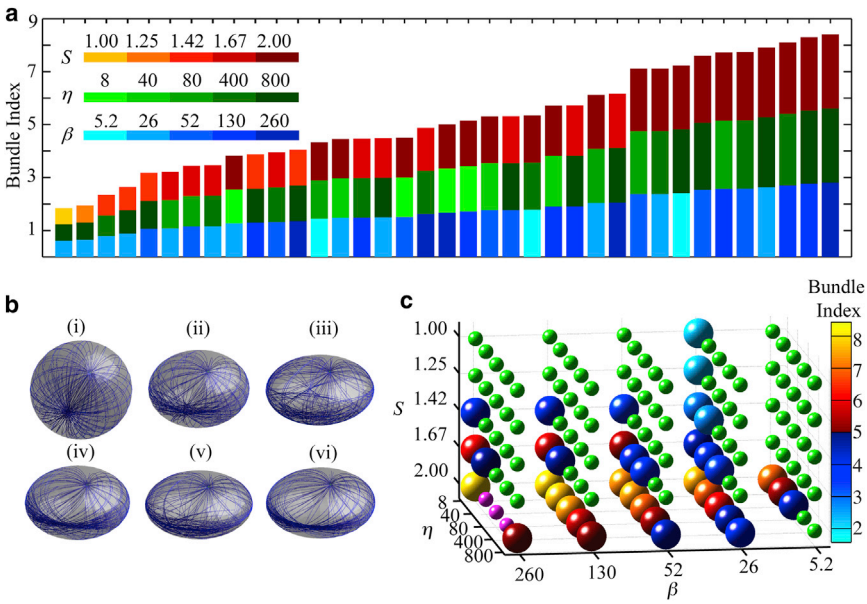

FIGURE 3 3D model parameter space of MT bundle formation. (*a*) MT bundle indices from 37 simulations sorted by index value (*bar height*), with colors indicating values of three parameters: cell-shape index (S), intracellular viscosity (η), and MT stiffness (β). (*b*) Final MT patterns for the selected cases $S = 1$, $\eta = 8$, $\beta = 26$, bundle index 1.85 (*i*); $S = 1.42$, $\eta = 8$, $\beta = 26$, bundle index 2.65 (*ii*); $S = 2$, $\eta = 800$, $\beta = 26$, bundle index 3.82 (*iii*); $S = 1.67$, $\eta = 8$, $\beta = 26$, bundle index 4.49 (*iv*); $S = 2$, $\eta = 800$, $\beta = 260$, bundle index 5.01 (*v*); and $S = 2$, $\eta = 8$, $\beta = 260$, bundle index 8.41 (*vi*); (*c*) 3D parameter space with color-coded MT bundle index. Large spheres indicate simulated results from Fig. 3 *a*, and small spheres represent the results for unsimulated cases, classified into bundled (*magenta spheres*) and unbundled (*green spheres*) for index threshold 5. The units of beta are [pN.μm^2], the units of eta are [pN.s/μm^2]. To see this figure in color, go online.

(Fig. 3 *c*, *large spheres*), with colors corresponding to the bundle index values, as in Fig. 3 *a*. By inspecting both the calculated bundle index and the MT patterns in each of the simulated cases (six representative MT configurations are shown in Fig. 3 *b*), we determined a threshold (set at 5) that separated the patterns with from those without MT bundles. The remaining cases (Fig. 3 *c*, *small spheres*) were classified based on the following observed correlations. Since the bundle index increases with decreasing values of intracellular viscosity (η) for fixed cell-shape index (S) and fixed MT stiffness (β), the three unsimulated cases for $S = 2$ must be bundled (bundle index >5, *magenta spheres*). For the same reasons, when all simulated cases for $S = 1.67$ and $S = 1.42$ are inspected along the η axis, the missing bundle indices must be <5 (unbundled). For fixed values of MT stiffness (β) and intracellular viscosity (η), the bundle index decreases with decreasing shape index (S), and thus, all unsimulated cases for $S = 1.25$ and $S = 1$ are unbundled (*green spheres*).

Cell shape and cytoplasm viscosity versus bundle index

Our analysis of the 3D model parameter space shown in Fig. 3 indicates that cell shape is a crucial factor in the formation of MT bundles. All stabilized MTs would grow as straight filaments if they were not confined to a limited space or blocked by intracellular obstacles (such as organelles). In our model, all MTs are confined to the cell boundary, and thus, as they grow longer, the MTs must bend to fit into the intracellular space. MT shape deformations are regulated by elastic energy minimization. It can be seen that when cell shape is ellipsoidal (oblate in the z axis in our model), MTs that run along the cell boundary are deformed by crossing the cell equator (largest horizontal cross section), thereby storing elastic energy, and that the more vertical the crossing angle, the more energy is stored. Therefore, the MTs will turn in the direction of their growing filaments, so that they run along the equator. The flatter the cell, the greater is the tendency of the MT to turn parallel to the equator to lower the stored elastic energy, because the latitude lines have larger principal curvature at the equator. Thus, the MT bundle index is an increasing function of the cell-shape index (S), as shown quantitatively in Fig. 4 (*dashed line*) for one specific combination of viscosity and stiffness parameters.

On the other hand, the MT bundle index decreases as intracellular viscosity values rise. Since the velocity at which the MT nodes are relocated is inversely proportional to intracellular viscosity (Eq. 1), this viscosity acts as a resistance against the relaxation of the deformed body (MT) in the surrounding media. The more viscous the cytoplasm, the longer it takes for a deformed MT to reach a relaxed state. When the MT is growing and its tip hits the cell boundary, the whole MT structure, from its tip to the clamped base, needs to respond by changing position. When intracellular viscosity is high, the MT deformation is slower and a new rod segment may be added at the tip before the whole MT reaches the relaxed state. Therefore, the MT aster in the medium of high viscosity has a less organized structure from the centrosome all the way to the tips (see Fig. 3 *c*, *iii*). This results in a lower MT bundle index. In Fig. 4, the MT bundle index is shown quantitatively as a decreasing function of intracellular viscosity, η, for two specific combinations of cell-shape and MT-stiffness parameters (*solid lines*).

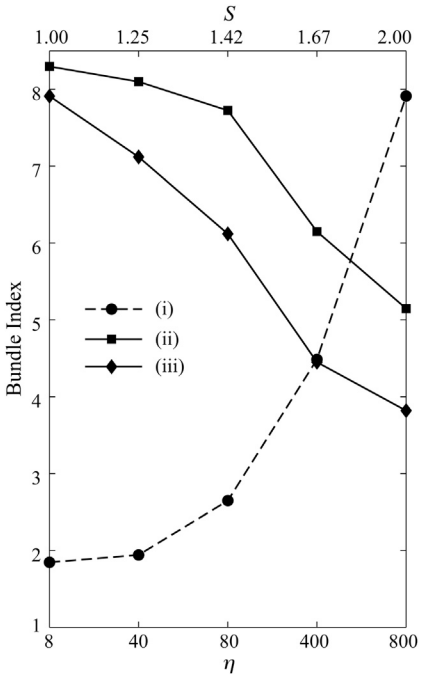

FIGURE 4 MT bundle index as a function of cytoplasmic viscosity or cell shape. Cell-shape index, S, is shown on the top axis and cytoplasmic viscosity, η, on the bottom axis. MT bundle index increases as a function of S when β and η are fixed, as in case i (*dashed line*; $\eta = 8$ and $\beta = 26$), and decreases as a function of η when S and β are fixed, as in cases ii and iii (*solid lines*), where $S = 2$ and $\beta = 130$ (*ii*) and $S = 2$ and $\beta = 26$ (*iii*). The units of beta are [pN.μm^2], the units of eta are [pN.s/μm^2].

MT stiffness and the bundle index

Our quantitative analysis of the simulated results from Fig. 3 *c* is presented in Fig. 5 *a* for four different sets of fixed S and η values. This graph indicates that the bundle index increases as a function of MT stiffness, β, which is a rather counterintuitive result. In our model, one end of each MT is clamped on the centrosome, but the other end has no physical constraints other than confinement within the cell boundary. Its movement is only restricted by the bending forces upon MT contact with the cell boundary. Thus, one would expect that it should be more difficult for the stiffer MTs to self-organize into parallel bundles.

To better understand the role of MT stiffness in bundle formation we compared two cases in which all parameters were identical except for MT stiffness, β. The cases considered are indicated in Fig. 5 (*red*, $\beta = 26$ pN·μm^2; *blue*, $\beta = 130$ pN·μm^2). Evolution of the bundle indices over time is shown for the two cases in Fig. 5 *b*, and the corresponding snapshots from the simulations, showing MT aster structure and WC values, are presented in Fig. 5 *c*. Initially, both bundle indices are equal to zero, since individual MTs are too distant from one another to form a bundle. The first positive contribution to the bundle index value takes place when MTs reach ~6 μm in length (Fig. 5 *b*), and the lower MT

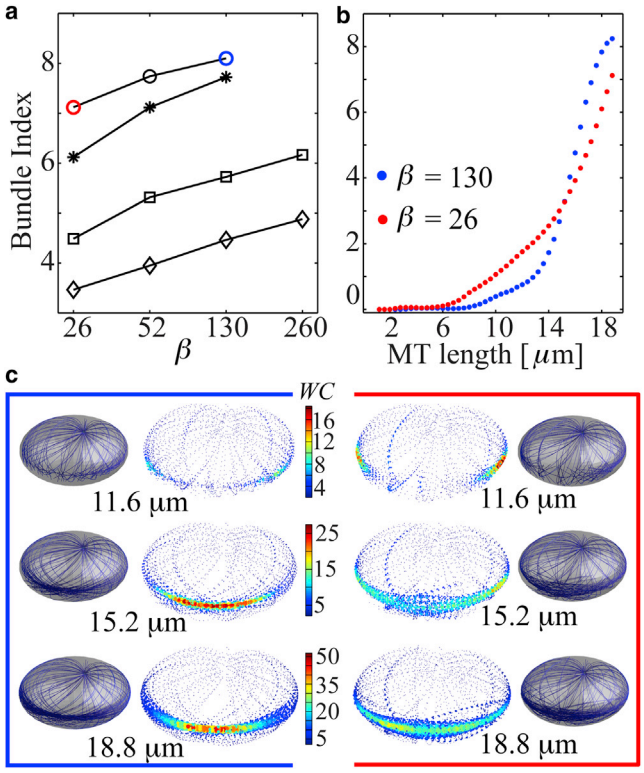

FIGURE 5 MT stiffness versus bundle index. (*a*) MT bundle index increases as a function of MT stiffness for $S = 2$ and $\eta = 40$ pN·s/μm^2 (*circles*), $S = 2$ and $\eta = 80$ pN·s/μm^2 (*stars*); $S = 1.67$ and $\eta = 8$ pN·s/μm^2 (*squares*); and $S = 1.43$ and $\eta = 8$ pN·s/μm^2 (*diamonds*). (*b*) Evolution of bundle indices as a function of the maximal length of growing MTs for two selected cases from *a*, indicated by red and blue circles. These two cases differ only in MT stiffness: $\beta = 130$ pN·μm^2 (*blue*) and $\beta = 26$ pN·μm^2 (*red*), with fixed $S = 2$ and $\eta = 40$ pN·s/μm^2. The *x*-axis labels can be converted to time by multiplying by 0.2 min/μm. (*c*) Snapshots from both simulations analyzed in *b*, showing comparison of MT aster structures and distributions of WC values. The color bars in the middle apply to both WC plots. See the corresponding simulation videos (Movies S3 and S4). To see this figure in color, go online.

stiffness (*red spheres*) results in a higher bundle index until they reach ~15 μm. This is an effect of MTs hitting the cell boundary during their growth, where the stiffer MTs move their free ends rather than bend the whole MT structure to comply with the impenetrability condition. This is confirmed by the corresponding snapshots in Fig. 5 *c*. For MTs of length 11.6 μm, higher WC values are observed in the lower MT stiffness case, because some MTs are bent along cell-surface contours. As the MTs grow longer, and many MT nodes are located along the cell boundary, the cell boundary contour becomes the preferred direction for rod segments newly added at the distal MT ends. In these cases, the stiffer MTs are aligned along the cell equator, contributing to higher bundle indices (Fig. 5 *c*, *middle* and *lower rows*). This is also evident from Fig. 5 *a* where the stiffer MTs curve (*blue*) increases in a much steeper way than the softer MTs curve (*red*) after the MTs reach

~13μm in length. A detailed comparison between changes in the shape of a single MT in both cases is presented in section S5 of the Supporting Material.

MT bundles in suspended versus attached cells

The patterns of MTs inside the CTCs suspended in the fluid environment of the blood might differ from those observed for captured or cultured tumor cells that are attached to the substrate. Thus far, we have considered only cases where cells are ellipsoidal in shape and do not deform during the simulations. In these cases the contour of the cell boundary along which the longitudinal principal curvature is lower provides guidance for growing MTs and leads to MT self-organization into a bundle. When the cells are attached, that is, they have an interface with the underlying substrate, we expect that the edge of this interface plays a role similar to that of the equator of an ellipsoid, as in the cases considered previously. However, cell attachment to the substrate can either precede or follow the taxane treatment, or the cells can actively attach during exposure to taxanes. We thus examined three scenarios in which the order of MT growth in taxane-treated cells and cell attachment to the substrate were altered (Fig. 6). In the first case (Fig. 6, *i*), the MTs were growing while the cell formed an attachment; in the second case (Fig. 6, *ii*), the MTs had already reached 18.8 μm in length before the cell started forming an attachment with the substrate; and in the last case (Fig. 6, *iii*), the MTs were growing in the already-attached cell. Our simulations were carried out for the cell of spherical shape ($S = 1$), which was previously shown to have a low MT bundle index regardless of the values of MT stiffness and intracellular viscosity. The attaching cell was modeled as a sphere undergoing truncation by gradually moving a horizontal plane (at the rate of 0.025 μm/s) from the bottom until it reached the equator (the largest horizontal cross section). Our goal was to determine how the planar part of a cell boundary influences the MT bundle index. The changes in MT bundle index values in all cases considered are shown in Fig. 6 together with the final MT configurations.

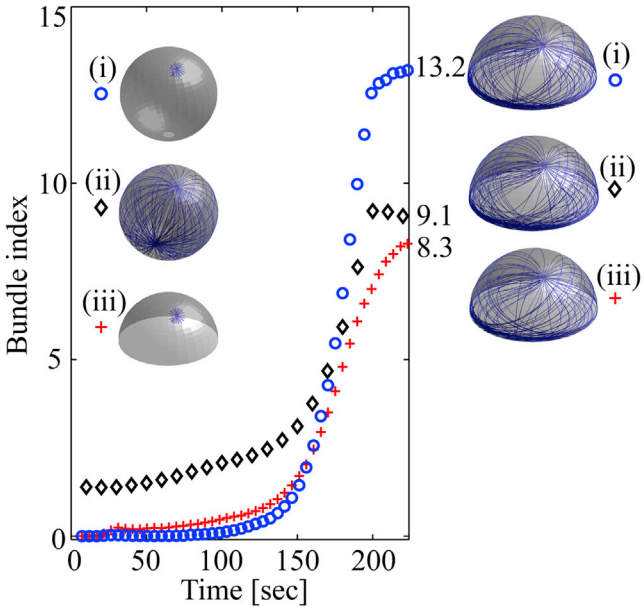

FIGURE 6 Dynamical changes in the MT bundle index in taxane-treated cells upon attachment to the substrate. Evolution of MT bundle index over time for the cases where MT growth and cell attachment occur in parallel (*i*, *blue circles*), attachment of the cell occurs after MT growth (*ii*, *black diamonds*); and attachment of the cell occurs before MT growth (*iii*, *red plus symbols*); final MT bundle indices and corresponding MT configurations are shown at right. (*Insets*) Initial MT configurations, where cell parameters are $\beta = 26$ pN$\cdot\mu$m^2, $\eta = 8$ pN$\cdot$s/μm^2, and $S = 1$. Accompanying simulations are shown in Movie S5. To see this figure in color, go online.

When comparing the three scenarios, case ii, in which MT growth precedes cell attachment, is characterized initially by a much higher bundle index, because the MTs are already grown. However, at later times, the bundle index from case ii is surpassed by that of case i, in which growth and cell attachment take place in parallel. In cases i and iii, both bundle indices take near-zero values for a long time. However, the bundle index in case iii is slightly higher than that in case i because the MTs in an already attached cell (Fig. 6, *iii*) hit the cell surface and the truncation corner earlier than those in case i. Moreover, as the MTs grow in parallel to cell attachment (Fig. 6 *i*), the MT spatial organization is gradually guided by the edge forming on the cell-truncation surface interface, leading to the emergence of a tight MT bundle. More details of these processes, and several corresponding snapshots are provided in section S6 of the Supporting Material and Movie S5.

Upon attachment of the cell to the surface, the sharp corner formed between the cell boundary and the truncation plane limits the direction of MT relaxation, creating a trap for the freely expanding MTs. This corner forces the trapped MTs to align along the truncation interface edge, allowing for bundle formation and resulting in a high MT bundle index. A similar trap is formed along the equators of ellipsoidal cells, where the latitudinal principal curvature is highest and the longitudinal principal curvature is lowest. Specifically, we consider the ellipsoid with a shape index of $S = 2$ and parameters β and η identical, as in Fig. 6. In this case, both the cell height (5 μm) and the cell radius (5 μm) are the same as in the fully attached cells in Fig. 6. However, the final bundle indices (13.2, 9.1, and 8.3) (Fig. 6) are higher than that in the ellipsoidal counterpart (7.91) (Fig. S1 *a*). The reason for such a difference in bundle index is the existence of the sharp corner along the truncation edge. In the case of the ellipsoidal cell, the equator is a smooth surface, across which MTs can slide as they grow. However, the MTs that grow inside the truncated cell follow the corner contour,

resulting in tighter bundle formation and a higher bundle index.

Comparison with experimental data

Experimentally, the MT bundles can be identified from immunofluorescence microscopy images of cells stained with antitubulin antibodies. An example of ovarian carcinoma cells exposed to taxane is shown in Fig. 7 *b*. A cell with well-developed MT bundles (*arrow*) is shown in contrast to cells with MTs that are not spatially localized (*arrowheads*). The existence of the MT bundle is usually determined by visual inspection and by comparison between the cells. Since the MT cross-section diameter is smaller than the optical wavelength, it is impossible to use fluorescent images to provide a quantitative measure of MT length or to determine more detailed MT spatial organization. Here, we developed a method for generating fluorescence-microscopy-like images from simulation outcomes of our mathematical model (Fig. 7 *a*), as well as a quantitative assessment of MT bundle structure from these images (Fig. 7 *c*). The following rendering method was used. Each MT segment was considered to be a light source that gave rise to a blur circle with a diameter proportional to its distance from the focal plane chosen to cut through the cell equator. Therefore, the more MTs that are bundled along the cell equator, the more focused and brighter the image created. The recorded light intensity is also proportional to the exposure time (Fig. 7 *a*, *ExpT*). This procedure is meant to simulate the 16-bit CCD sensor recording.

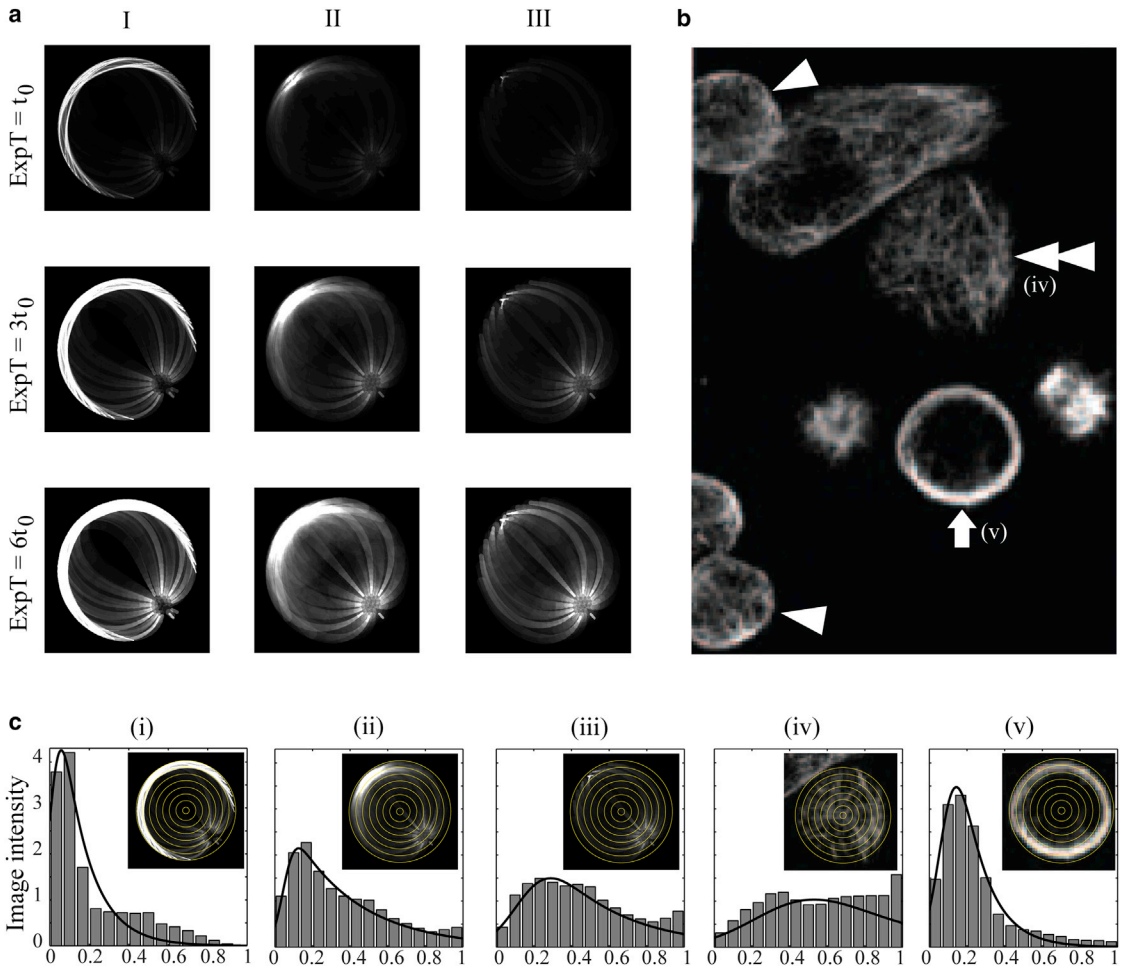

FIGURE 7 Fluorescent imaging and computational rendering of MT bundles. (*a*) Computational fluorescent-like rendering of images with three exposure times (ExpT = t_0, $3t_0$, and $6t_0$) from three previously discussed simulations with common parameters $\beta = 26$ pN·μm^2 and $\eta = 8$ pN·s/μm^2 and variable parameters $S = 2.00$ and MT length 18.8μm (*I*), $S = 1.00$ and MT length 18.8μm (*II*), and $S = 1.00$ and MT length 9.6μm (*III*). The corresponding bundle indices are 7.91 (*I*), 1.85 (*II*), and 0.42 (*III*). (*b*) An immunofluorescence microscopy image of 1A9 human ovarian carcinoma cells after 24 h exposure to taxane, from Marcus et al. (5). All cells are stained with an antitubulin antibody showing the MT bundle (*arrow*) or MT meshwork, indicating the lack of visible bundles (*arrowheads*). (*c*) Quantitative analysis of the averaged MT image intensity distributions and the exponentially modified Gaussian curves, with the following fitted parameters (μ, σ, λ): (*i*) (0.30, 0.25, 2.35), (*ii*) (0.07, 0.06, 7.29), (*iii*) (0.004, 0.04, 7.34), (*iv*) (0.05, 0.05, 2.86), and (*v*) (0.13, 0.13, 2.66). Insets in *i–iii* correspond to I–III, ExpT = $3t_0$, and those in *iv* and *v* correspond to IV and V from *b*. The *x* axes in each histogram represent the relative position of each ring normalized by the cell radius. To see this figure in color, go online.

The results of applying our rendering method to one bundled and two unbundled computational cases are shown in Fig. 7 *a* for three different ExpT values (sixfold difference). For the bundled case presented in column I (bundle index 7.91), the rendering method showed a well-defined bright ring around the cell periphery for each ExpT value. On the other hand, for the unbundled case presented in column II (bundle index 1.85), the partial ring along the cell periphery is visible only when the exposure time is long enough. However, the central area of these images becomes quite fuzzy, in contrast to those of the images in column I. As a control case, we considered a cell with MTs that are too short to form a bundle (bundle index 0.42). The rendered images in column III show a quite uniform gray pattern, even for the longest ExpT. These results of our fluorescence-microscopy-like image rendering indicate that it is important to consider different exposure times, so that the localized MTs are clearly visible, without too much saturation of nonlocalized MTs that might mislead the observer. This tradeoff between the exposure and saturation is characteristic of all fluorescence microscopy systems. Among the results presented in Fig. 7 *a*, ExpT $= 3t_0$ is our best pick.

With the chosen exposure time (ExpT $= 3t_{0)}$, we performed further analysis to provide a quantitative way to compare both computational and experimental images of cells with fluorescently stained MTs. Fig. 7 *c* shows three examples of computational cells (*i–iii*) from Fig. 7 *a* and two examples of experimental cells from Fig. 7 *b* (*iv* and *v*, *double arrowhead* and *arrow*). The averaged MT image intensity distributions for each cell were taken over the concentric rings imposed on the cell image and normalized by cell diameter (Fig. 7 *c*). We used 15 concentric rings, starting on the cell periphery and gradually progressing toward the cell center; for visual clarity, only 8 of 15 rings are shown (Fig. 7 *c*, *i–v*, *insets*). These MT intensity data were fitted (Fig. 7 *c*, *solid lines*) using the exponentially modified Gaussian distribution (EMG) with probability density function *f*, defined as (34)

$$f(x;\mu,\sigma,\lambda) = 0.5\lambda \times \exp\left(\lambda\left(2\mu+\lambda\sigma^2-2x\right)/2\right) \times \operatorname{erfc}\left(\left(\mu+\lambda\sigma^2-x\right)/\left(\sqrt{2}\sigma\right)\right), \quad (7)$$

where erfc is the complementary error function and (μ, σ, λ) are the mean and standard deviation of the Gaussian component and the rate of the exponential component, respectively. These three coefficients are used as the fitting parameters.

These quantitative results confirm our visual inspection of the analyzed images. The distributions in bundled cases (Fig. 7 *c*, *i* and *v*) are characterized by relatively high peaks skewed to the left, that is, toward the cell periphery. In both cases, the mean values, μ, are low, and the parameters σ and λ, which measure whether the distribution is concentrated around its mean (low σ and high λ), are similar, (0.004, 0.04, 7.34) and (0.07, 0.06, 7.23), respectively. The distributions of two unbundled cells (Fig. 7 *c*, *iii* and *iv*) are quite similar as well and exhibit a more uniform pattern (high σ and low λ), with insignificant peaks located near the center (high μ). The distribution in Fig. 7 *c*, *ii*) has mixed characteristics, with μ and σ very close to those of case i but λ close to that of case iii. From the statistical characteristics of EMG, with mean and variance of $\mu + 1/\lambda$ and $\sigma^2 + 1/\lambda^2$, respectively, it is clear that near-periphery μ, low σ, and high λ are required to produce intensity values concentrated around the cell edge, identified as the MT bundle, with low intensity in the cell center, as in Fig. 7 *c*, *i* and *v*.

DISCUSSION AND CONCLUSIONS

Simple biological structures, such as rod-shaped MTs, actin filaments, or cilia, can be organized into complex feature-rich patterns via their interactions with one another and with the surrounding media. In this article, we adapted a previously developed model of MT dynamics inside the cell, and we show that the MT stabilization and cell-boundary curvature gradient influence the formation of bundle-like structures without global pattern-organizing guidance. To define and analyze the MT bundling phenomenon in a quantitative way, we developed the bundle index idea. This proprietary measure was applied to our simulations, and we show that it is in accordance with the biological concept of bundling as determined from fluorescent staining. Using our model and the bundle-index metrics, we investigated the roles of three properties in MT bundle formation: MT stiffness, intracellular viscosity, and cell shape. It has been reported that taxane treatment not only stabilizes MTs but may also modify their stiffness (29,30,35,36). We took this into consideration by varying the MT bending rigidity parameter, β. To account for physical properties of the intracellular environment in which the MTs live, we defined the model governing equations based on fluid-structure interface methods, in which the intracellular viscosity, η, is a crucial parameter determining overall MT behavior. We thus varied this parameter according to experimentally measured values of intracellular (effective) viscosity (31–33,37–41). The cell deformation index, *S*, which defines cell shape has been varied to consider the steepness of the curvature gradient on the oblate spheroid, as it played a key role in MT bundle formation. Through our simulation study, we show that the MT bundle index in ellipsoidal cells increases as MTs stiffen, intracellular viscosity thickens, and cell shape becomes more flattened. We also investigated the MT rearrangement in both suspended and attached cells. Specifically, we studied the effects of cell attachment to the substrate on the MT aster. Our simulations reveal that the time of cell exposure to taxanes (before, during, or after formation of attachments) can impact MT bundling. This may guide further experimentation to minimize side effects of investigating drug effectiveness in the attached cells.

Finally, our fluorescence-microscopy-like image rendering closely reproduced the heterogeneous MT patterns observed in cells exposed to taxanes. As shown in Fig. 7 *b*, cells derived from the same tumorigenic cell line and exposed to a uniform drug concentration in culture can respond in different ways, with some forming an MT bundle and others not. Our image-rendering technique, coupled with a mechanical model of MT rearrangement, provided a physical explanation for this heterogeneity. Investigating the conditions in which taxane-treated cells do not form MT bundles is important in the light of recent experimental findings (reviewed in Thadani-Mulero et al. (42)) indicating that spatial localization of MTs may be involved in the inhibition of certain signaling and trafficking pathways that affect the clinical efficacy of taxanes.

In summary, using our computational approach, we showed that biophysical properties of the cell such as cell deformation (shape), intracellular viscosity, and MT stiffness, can affect formation of the MT bundle. We showed that the variability in cell biophysical properties or in experimental conditions (whether cells are in suspension or in contact with the substrate) can explain heterogeneity of the observed MT image patterns in cells treated with taxanes. Moreover, the developed fluorescent image rendering can provide a quantitative way to assess MT bundle formation from widely available fluorescent images. Thus, the quantitative procedures presented here can be useful in developing new methodologies for assessing treatment effectiveness based on physical measurements in individual cancer cells.

SUPPORTING MATERIAL

Six figures and five movies are available at http://www.biophysj.org/biophysj/supplemental/S0006-3495(14)00725-5.

This work was supported by the Physical Sciences-Oncology Center (PSOC) at the National Institutes of Health via the PSOC Trans-Network Project, an agreement with Cornell University Nanobiotechnology Center under 5U54-CA-143876-03, and Moffitt-PSOC grant U54-CA-143970.

REFERENCES

1. Heuser, J. E., and M. W. Kirschner. 1980. Filament organization revealed in platinum replicas of freeze-dried cytoskeletons. *J. Cell Biol.* 86:212–234.
2. Hirokawa, N. 1982. Cross-linker system between neurofilaments, microtubules, and membranous organelles in frog axons revealed by the quick-freeze, deep-etching method. *J. Cell Biol.* 94:129–142.
3. Azarenko, O., T. Okouneva, …, L. Wilson. 2008. Suppression of microtubule dynamic instability and turnover in MCF7 breast cancer cells by sulforaphane. *Carcinogenesis.* 29:2360–2368.
4. Burgin, K. E., B. Ludin, …, A. Matus. 1994. Bundling of microtubules in transfected cells does not involve an autonomous dimerization site on the MAP2 molecule. *Mol. Biol. Cell.* 5:511–517.
5. Marcus, A. I., U. Peters, …, P. Giannakakou. 2005. Mitotic kinesin inhibitors induce mitotic arrest and cell death in Taxol-resistant and -sensitive cancer cells. *J. Biol. Chem.* 280:11569–11577.
6. Takamori, N., A. Shimomura, and T. Senda. 2006. Microtubule-bundling activity of APC is stimulated by interaction with PSD-95. *Neurosci. Lett.* 403:68–72.
7. Weisshaar, B., T. Doll, and A. Matus. 1992. Reorganisation of the microtubular cytoskeleton by embryonic microtubule-associated protein 2 (MAP2c). *Development.* 116:1151–1161.
8. Dumontet, C., and M. A. Jordan. 2010. Microtubule-binding agents: a dynamic field of cancer therapeutics. *Nat. Rev. Drug Discov.* 9:790–803.
9. Jordan, M. A., and K. Kamath. 2007. How do microtubule-targeted drugs work? An overview. *Curr. Cancer Drug Targets.* 7:730–742.
10. Jordan, M. A., and L. Wilson. 2004. Microtubules as a target for anticancer drugs. *Nat. Rev. Cancer.* 4:253–265.
11. Amos, L. A., and J. Löwe. 1999. How Taxol stabilises microtubule structure. *Chem. Biol.* 6:R65–R69.
12. Arnal, I., and R. H. Wade. 1995. How does taxol stabilize microtubules? *Curr. Biol.* 5:900–908.
13. Goodsell, D. S. 2000. The molecular perspective: microtubules and the taxanes. *Oncologist.* 5:345–346.
14. Darshan, M. S., M. S. Loftus, …, P. Giannakakou. 2011. Taxane-induced blockade to nuclear accumulation of the androgen receptor predicts clinical responses in metastatic prostate cancer. *Cancer Res.* 71:6019–6029.
15. Ganguly, A., H. Yang, and F. Cabral. 2010. Paclitaxel-dependent cell lines reveal a novel drug activity. *Mol. Cancer Ther.* 9:2914–2923.
16. Kirby, B. J., M. Jodari, …, P. Giannakakou. 2012. Functional characterization of circulating tumor cells with a prostate-cancer-specific microfluidic device. *PLoS ONE.* 7:e35976.
17. Andergassen, U., A. C. Kölbl, …, U. Jeschke. 2013. Detection of circulating tumour cells from blood of breast cancer patients via RT-qPCR. *Cancers* (*Basel*). 5:1212–1220.
18. Danila, D. C., G. Heller, …, H. I. Scher. 2007. Circulating tumor cell number and prognosis in progressive castration-resistant prostate cancer. *Clin. Cancer Res.* 13:7053–7058.
19. Hsieh, H. B., D. Marrinucci, …, J. Nieva. 2006. High speed detection of circulating tumor cells. *Biosens. Bioelectron.* 21:1893–1899.
20. Marrinucci, D., K. Bethel, …, P. Kuhn. 2012. Fluid biopsy in patients with metastatic prostate, pancreatic and breast cancers. *Phys. Biol.* 9:016003.
21. Nieva, J., M. Wendel, …, P. Kuhn. 2012. High-definition imaging of circulating tumor cells and associated cellular events in non-small cell lung cancer patients: a longitudinal analysis. *Phys. Biol.* 9:016004.
22. Scher, H. I., X. Jia, …, G. Heller. 2009. Circulating tumour cells as prognostic markers in progressive, castration-resistant prostate cancer: a reanalysis of IMMC38 trial data. *Lancet Oncol.* 10:233–239.
23. Ahmed, A. A., X. Wang, …, R. C. Bast, Jr. 2011. Modulating microtubule stability enhances the cytotoxic response of cancer cells to Paclitaxel. *Cancer Res.* 71:5806–5817.
24. Kim, M. J., and I. V. Maly. 2009. Deterministic mechanical model of T-killer cell polarization reproduces the wandering of aim between simultaneously engaged targets. *PLOS Comput. Biol.* 5:e1000260.
25. Cytrynbaum, E. N., J. M. Scholey, and A. Mogilner. 2003. A force balance model of early spindle pole separation in *Drosophila* embryos. *Biophys. J.* 84:757–769.
26. Nédélec, F. 2002. Computer simulations reveal motor properties generating stable antiparallel microtubule interactions. *J. Cell Biol.* 158:1005–1015.
27. Gamblin, T. C., K. Nachmanoff, …, R. C. Williams, Jr. 1996. Recombinant microtubule-associated protein 2c reduces the dynamic instability of individual microtubules. *Biochemistry.* 35:12576–12586.
28. Pedigo, S., and R. C. Williams, Jr. 2002. Concentration dependence of variability in growth rates of microtubules. *Biophys. J.* 83:1809–1819.
29. Hawkins, T., M. Mirigian, …, J. L. Ross. 2010. Mechanics of microtubules. *J. Biomech.* 43:23–30.

30. Tuszyński, J. A., T. Luchko, …, J. M. Dixon. 2005. Anisotropic elastic properties of microtubules. *Eur. Phys. J. E Soft Matter.* 17:29–35.

31. Daniels, B. R., C. M. Hale, …, D. Wirtz. 2010. Differences in the microrheology of human embryonic stem cells and human induced pluripotent stem cells. *Biophys. J.* 99:3563–3570.

32. Laurent, V. M., E. Planus, …, D. Isabey. 2003. Mechanical assessment by magnetocytometry of the cytosolic and cortical cytoskeletal compartments in adherent epithelial cells. *Biorheology.* 40:235–240.

33. Taylor, E. W. 1965. Brownian and saltatory movements of cytoplasmic granules and the movement of anaphase chromosomes. *Proc. Int. Cong. Rheol. Symp. Biorheol., 4th.* 175–191.

34. Grushka, E. 1972. Characterization of exponentially modified Gaussian peaks in chromatography. *Anal. Chem.* 44:1733–1738.

35. Mickey, B., and J. Howard. 1995. Rigidity of microtubules is increased by stabilizing agents. *J. Cell Biol.* 130:909–917.

36. VanBuren, V., L. Cassimeris, and D. J. Odde. 2005. Mechanochemical model of microtubule structure and self-assembly kinetics. *Biophys. J.* 89:2911–2926.

37. Bausch, A. R., W. Möller, and E. Sackmann. 1999. Measurement of local viscoelasticity and forces in living cells by magnetic tweezers. *Biophys. J.* 76:573–579.

38. Kole, T. P., Y. Tseng, …, D. Wirtz. 2004. Rho kinase regulates the intracellular micromechanical response of adherent cells to rho activation. *Mol. Biol. Cell.* 15:3475–3484.

39. Lee, J. S., P. Panorchan, …, D. Wirtz. 2006. Ballistic intracellular nanorheology reveals ROCK-hard cytoplasmic stiffening response to fluid flow. *J. Cell Sci.* 119:1760–1768.

40. Tsai, M. A., R. S. Frank, and R. E. Waugh. 1993. Passive mechanical behavior of human neutrophils: power-law fluid. *Biophys. J.* 65:2078–2088.

41. Tseng, Y., T. P. Kole, and D. Wirtz. 2002. Micromechanical mapping of live cells by multiple-particle-tracking microrheology. *Biophys. J.* 83:3162–3176.

42. Thadani-Mulero, M., D. M. Nanus, and P. Giannakakou. 2012. Androgen receptor on the move: boarding the microtubule expressway to the nucleus. *Cancer Res.* 72:4611–4615.